Presentation of the dynamical core of neXtSIM, a new sea ice model

Sylvain Bouillon, Pierre Rampal

Presentation of the dynamical core of neXtSIM, a new sea ice model

Sylvain Bouillon[a,b], Pierre Rampal[a,b]

[a] *Nansen Environmental and Remote Sensing Center, Bergen, Norway*
[b] *Bjerknes Centre for Climate Research, Bergen, Norway*

Abstract

The dynamical core of a new sea ice model is presented. It is based on the Elasto-Brittle rheology, which is inspired by progressive damage models used for example in rock mechanics. The main idea is that each element can be damaged when the local internal stress exceeds a Mohr-Coulomb failure criterion. The model is implemented with a finite element method and a Lagrangian advection scheme. Simulations of 10 days are performed over the Arctic at a resolution of 7 km. The model, which has only a few parameters, generates discontinuous sea ice velocity fields and strongly localized deformation features that occupy a few percent of the total sea ice cover area but accommodate most of the deformation. For the first time, a sea ice model is shown to reproduce the multifractal scaling properties of sea ice deformation. The sensitivity to model parameters and initial conditions is presented, as well as the ability of the Lagrangian advection scheme at preserving discontinuous fields.

Keywords: sea ice model, Lagrangian, rheology, multifractal scaling, Arctic

---

Email address: `sylvain.bouillon@nersc.no` (Sylvain Bouillon)

1. Introduction

Sea ice dynamics, and more specifically its brittle deformation, exhibit scale invariance properties in both the temporal and spatial domains (Marsan and Weiss, 2010; Weiss, 2013). Scale invariance is a frequent characteristic of dynamical systems where energy introduced at large scale is redistributed towards smaller scales, down to the dissipation scale (e.g., the development of turbulence down to the viscous dissipation scale). In the case of sea ice, the kinetic energy is mainly coming from the wind stress, which varies over typical time and length scales $T_{wind} \approx 3 - 6$ days and $L_{wind} \approx 100 - 1000$ km, respectively. A large part of this energy is transferred to the ocean but a non-negligible part is dissipated by friction during sea ice fracturing events. These events last a few minutes (Marsan et al., 2011) and occur along faults of tens of meters (Schulson, 2004). Above this dissipation scale, sea ice drift and deformation show scaling properties over several orders of magnitude, from a few hours to a few months, and from hundreds of meters to hundreds of kilometers (Marsan et al. (2004), Rampal et al. (2008)). These properties are in fact quite universal in complex dynamical systems and are likely to emerge from the interaction of a large number of components rather than from a specific process occurring at small scales. This explains for example why simplistic models such as random fuse or random spring models are capable of reproducing complex statistical properties observed for failure in disordered materials, e.g. damage localization and power law distribution of avalanche size (Nukala et al., 2005). The external forcing is one source of scaling in the sea ice dynamics, and should become predominant as the ice cover is more fractured. However, the statistical properties of sea ice dynamics differ from those of ocean and atmosphere dynamics (Rampal et al., 2009). An important characteristic of sea ice dynamics is the multifractality of the scale invariance of sea ice deformation (Weiss and Marsan, 2004), which seems to emanate from the intrinsic properties of solid materials characterized by brittle mechanical behavior (Weiss, 2013).

To correctly reproduce scale invariance properties of sea ice dynamics may be important to better understand the exchanges of energy between the ocean and the atmosphere, which are highly influenced by the opening and closing of leads in the ice cover. In winter, deformation contributes to about 25-40% of the ice production (Kwok, 2006) and the presence of leads, which cover only a few percent of the domain, may account for more than 70% of the upward heat fluxes (Marcq and Weiss, 2012) and for half the salt rejection (Morison and McPhee, 2001). To correctly forecast sea ice motion and deformation would also give crucial information (e.g. the presence of ridges) for ship operations in ice covered areas. Therefore, we think that sea ice models used for forecasting and climate studies should be also evaluated regarding their ability to reproduce the statistical properties of sea ice drift and deformation.

This paper presents the dynamical core of a new sea ice model called neXtSIM, which is based on an innovative mechanical modeling framework. Sea ice dynamics are simulated using an adapted and optimized version of the Elasto-Brittle rheology originally presented in Girard et al. (2011), which initially was inspired by a progressive damage model used to simulate rock mechanics (Amitrano et al., 1999). The main ingredients of this dynamical sea ice model are detailed, and the ability of the model to generate sea ice deformation fields having correct statistical and scaling properties is demonstrated. An extensive sensitivity study is performed to evaluate the pertinence of each key ingredient of the model. In section 2 we present the main equations of the model. Section 3 describes how these equations are discretized in space and time and which advection scheme the model uses. Section 4 shows the results of a reference simulation of 10 days over the central Arctic, for which we also present a sensitivity analysis with respect to initial conditions and to some key sea ice mechanical parameters. Note that for short time scale simulations, we assume the impact of thermodynamical processes on the dynamics as being negligible. This study is the first step towards a more complete presentation of neXtSIM, in which e.g. sea ice thermodynamics should be implemented. We do not present a comparison of the simulated fields to observed fields in order to keep this paper focused on the description of the model and to make it accessible to a large scientific audience. The evaluation of the predictive skill of the model or its impact on other components of the climate system is therefore out of scope of this paper.

2. Model description

At the present stage, the dynamical component of neXtSIM is kept as simple as possible and has only five prognostic variables. h, hereafter called sea ice thickness, is the volume of ice per unit area and A, hereafter called sea ice concentration, is the surface of ice per unit area. $\boldsymbol{u}$ is defined as the horizontal sea ice velocity and $\boldsymbol{\sigma}$ is the internal stress tensor. The damage d is a non-dimensional scalar variable, which is equal to 0 for undamaged material and to 1 for completely damaged material.

One of the objectives for the model is to reproduce the failure zones that are observed from satellites at a resolution of 10 km. As in Hutchings et al. (2005), we assume that sea ice is heterogeneous at the scale of the model, which corresponds to its resolution Δx (here about 10 km). The sea ice thickness, concentration, damage, internal stress and deformation rate tensors are defined for each element and could strongly vary from one element to the next one. The velocities are defined at the corners of each element. Our model is continuous and uses a Lagrangian approach, i.e. while the nodes are moving accordingly to the ice motion the elements remain connected and always cover the same domain. Eulerian approaches might also be used but then one should use advection schemes that are able to transport highly heterogeneous fields while conserving the extreme gradients present at the scale of the elements.

2.1. Evolution of sea ice thickness, concentration and velocity

The evolution equations for sea ice thickness, concentration and velocity are similar to those used in most sea ice models. When the thermodynamics terms are neglected, the evolution of h and A are given by:

$$\frac{Dh}{Dt} = -h\nabla \cdot \boldsymbol{u}, \tag{1}$$

$$\frac{DA}{Dt} = -A\nabla \cdot \boldsymbol{u}, \tag{2}$$

where $\frac{D\phi}{Dt}$ is the material derivative of ϕ (being either a scalar or a vector). A is limited to a maximum value of 1.

The evolution of sea ice velocity comes from the vertically integrated sea ice momentum equation :

$$\rho_i h \frac{D\boldsymbol{u}}{Dt} = \nabla \cdot (\boldsymbol{\sigma} h) + A(\boldsymbol{\tau}_a + \boldsymbol{\tau}_w) - \rho_i h f \boldsymbol{k} \times \boldsymbol{u} - \rho_i h g \nabla \eta, \tag{3}$$

where ρ_i is the ice density, $\boldsymbol{\tau}_a$ and $\boldsymbol{\tau}_w$ are the surface wind (air) and ocean (water) stresses, respectively, f is the Coriolis parameter, $\boldsymbol{k}$ is the upward pointing unit vector, g is the gravity acceleration and η is the ocean surface elevation.

It should be noted that in the sea ice community the term internal stress often refers to the vertically integrated (or depth-integrated) internal stress, which has units of Nm^{-1}. Such a definition may lead to confusion as in Girard et al. (2011) where the integrated internal stress (in Nm^{-1}) was compared to cohesion and tensile strength defined in Nm^{-2} (Pa). To avoid confusion, we introduce the integration of the internal stress $\boldsymbol{\sigma}$ (in Nm^{-2}) in the momentum equation as in Sulsky et al. (2007). The internal stress is assumed to be homogeneously distributed in the ice volume and $\boldsymbol{\sigma} h$ corresponds to the integral of the internal stress within that volume.

The surface wind (air) and ocean (water) stresses, $\boldsymbol{\tau}_a$ and $\boldsymbol{\tau}_w$ respectively, are both multiplied by the sea ice concentration as in Connolley et al. (2004) and Hunke and Dukowicz (2003). The air stress $\boldsymbol{\tau}_a$ is computed following the quadratic expression:

$$\boldsymbol{\tau}_a = \rho_a c_a \left|\boldsymbol{u}_a\right| \left[\boldsymbol{u}_a \cos\theta_a + \boldsymbol{k} \times \boldsymbol{u}_a \sin\theta_a\right], \tag{4}$$

where $\boldsymbol{u}_a$ is the air velocity, ρ_a the air density, θ_a the air turning angle and c_a the air drag coefficient. The water stress $\boldsymbol{\tau}_w$ is computed following the quadratic expression:

$$\boldsymbol{\tau}_w = \rho_w c_w \left|\boldsymbol{u}_w - \boldsymbol{u}\right| \left[(\boldsymbol{u}_w - \boldsymbol{u})\cos\theta_w + \boldsymbol{k} \times (\boldsymbol{u}_w - \boldsymbol{u})\sin\theta_w\right], \tag{5}$$

where $\boldsymbol{u}_w$ is the ocean velocity, ρ_w the reference density of seawater, θ_w the water turning angle and c_w the water drag coefficient.

2.2. Evolution of sea ice internal stress and damage

The evolution of sea ice internal stress and damage is based on three main ingredients: the linear elasticity, the failure envelope and the link between local damage and internal stress.

2.2.1. Linear elasticity

Assuming planar stress and linear elasticity as in Girard et al. (2011), Hooke's law in matrix notation (see for example Bower (2011) for a reference textbook) is given by:

$$\begin{bmatrix} \sigma_{11} \\ \sigma_{22} \\ \sigma_{12} \end{bmatrix} = \frac{E(A,d)}{(1-\nu^2)} \begin{bmatrix} 1 & \nu & 0 \\ \nu & 1 & 0 \\ 0 & 0 & \frac{1-\nu}{2} \end{bmatrix} \begin{bmatrix} \epsilon_{11} \\ \epsilon_{22} \\ 2\epsilon_{12} \end{bmatrix}, \tag{6}$$

where $E(A,d)$ is the effective elastic stiffness, which here is assumed to depend on the concentration and damage. ν is Poisson's ratio, which is set here to 0.3, which is in the range of value discussed in Mellor (1986). To simplify notation, equation 6 may also be written in tensor notation as:

$$\boldsymbol{\sigma} = \boldsymbol{C}(A,d) : \boldsymbol{\epsilon}, \tag{7}$$

and in index notation as: $\sigma_{ij} = C_{ijkl}\epsilon_{kl}$.

The deformation response is then controlled by the effective elastic stiffness, which is defined as:

$$E(A,d) = Y f(A)(1-d), \tag{8}$$

where Y is the sea ice elastic modulus (Young's modulus) and $f(A)$ is a function equal to 1 when $A = 1$. This formulation of the effective elastic stiffness is similar to the one proposed in Girard et al. (2011) except that the linear dependence to h is now explicitly described in the momentum equation by the integration of the internal stress, and that we use a different convention for the damage d, which is equal to 0 for undamaged sea ice and to 1 for completely damaged sea ice.

Unlike in Girard et al. (2011) where the Young's modulus was tuned (to 0.35 GPa) to get the right order of magnitude for the mean total deformation, here we obtain realistic mean deformation when using a value of 9 GPa, i.e. in the range of in-situ measurements (Schulson, 2009). The value of the Young modulus does not affect the value of the cohesion, nor the failure envelope. It does not impact the magnitude of the internal stress but only the link between the internal stress and elastic deformation, the latter being much smaller than the observed deformation. Changing the value of the Young modulus modifies the elastic deformation but has no other significant impacts as long as we set it to a high enough value. This was checked by running a series of experiments with Y set to 9, 0.9 and 0.09 GPa respectively.

The impact of the concentration on the effective elastic stiffness is not known and thus has to be parameterized. We assume that for low values of concentration, the effective stiffness should be very low so that deformation could arise without impacting the internal stress. In this study, we use the same parameterization as in Girard et al. (2011):

$$f(A) = e^{\alpha(1-A)}, \tag{9}$$

where $\alpha \leq 0$ is a constant parameter. The sensitivity of the model to this parameter is presented in section 4. This function is similar to the one used in standard VP rheologies to parameterize the effect of the concentration on the ice strength P, which determines the size of the plastic envelop (Hibler, 1979). In our case, sea ice concentration has no impact on the failure envelope, which is determined instead by the cohesion parameter. In the future, more elaborate parameterization based on energetic considerations (Thorndike et al., 1975) or on simulations with ensemble of floes (Herman, 2013) may be needed to increase the realism of the model results. Another difference with the plastic approach is the absence of flow rule. Defining a flow rule for sea ice is questionable since sea ice does not behave plastically in the von Mises sense of plasticity (Weiss et al., 2007). In our case, defining a flow rule is not necessary as the model assumes that the ice deforms as an elastic medium (linearly with respect to the external force), whose elastic stiffness evolves over time.

2.2.2. Failure envelope

In-situ measurements made by Richter-Menge et al. (2002) indicate that sea ice internal stresses remains in an envelope, which is well represented by a combination of a Mohr-Coulomb criterion, a tensile stress criterion and a compressive stress criterion (see Figure 2 in Weiss et al. (2007)).

The Mohr-Coulomb criterion is defined by:

$$\tau \leq -\mu\sigma_N + c, \tag{10}$$

where μ is the friction coefficient and c is the cohesion, which is assumed to be always greater than 0 in the following discussion. The shear stress τ and the normal stress σ_N (also called tensile/compressive stress when it is positive/negative) are two invariants of the internal stress tensor and are defined by:

$$\tau = \sqrt{\left(\frac{\sigma_{11} - \sigma_{22}}{2}\right)^2 + \sigma_{12}^2}, \tag{11}$$

$$\sigma_N = \frac{\sigma_{11} + \sigma_{22}}{2}. \tag{12}$$

The tensile stress criterion and the compressive stress criterion are defined by:

$$\sigma_N \leq \sigma_{Nmax}, \tag{13}$$

and

$$\sigma_N \geq \sigma_{Nmin}, \tag{14}$$

where $\sigma_{Nmax} > 0$ and $\sigma_{Nmin} < 0$ are the maximal tensile stress and the maximal compressive stress, respectively. Of course, σ_{Nmax} has to be lower than $\frac{1}{\mu}c$ to be effective.

As in Girard et al. (2011), the friction coefficient μ for sea ice is chosen equal to 0.7, which is a common value for geo-materials (Amitrano et al., 1999). This value is consistent with results from laboratory tests (Schulson et al., 2006) and seems to be scale-independent (Weiss and Schulson, 2009).

In contrast, the value of the cohesion c depends on the spatial scale (Weiss et al., 2007) according to the following relationship:

$$\frac{c_1}{c_2} \approx \left(\frac{l_2}{l_1}\right)^{0.5}, \tag{15}$$

where l_1 and l_2 correspond to the estimated size of the stress concentrator at two different scales (Schulson, 2004). At the laboratory scale (a few centimeters), the cohesion is estimated to be about 1 MPa, whereas in-situ measurements (scale of a few meters, $l = 1$) give a value of about 40 kPa (Weiss et al., 2007). By using the scaling relationship (equation 15) and assuming that the maximum size of stress concentrators "seen" by our model is equal to the resolution Δx (here about 10 km), the maximum value for the cohesion parameter c is set to 8 kPa. In order to study the sensitivity of the model to the cohesion parameter c (see section 4), we arbitrary define a set of plausible values for c (8, 4, 2, 1 and 0.5 kPa). These values for c correspond to stress concentrator sizes ranging from 10 km to 25 m. It should be noted that in our case all the elements have the same value for the cohesion. To randomly draw the value of the cohesion from a uniform distribution as done in Girard et al. (2011) does not seem to be necessary for a realistic set up (i.e., complex geometry, initial conditions and forcings). We tested that using a cohesion that is uniformly distributed between 0.5 c and 1.5 c produces similar results than using a constant value c.

The maximal tensile stress and maximal compressive stress should scale in the same way as c (Schulson, 2009). From in-situ measurements, Weiss et al. (2007) estimated the maximal tensile stress σ_{Nmax} as equal to 50 kPa and the maximal compressive stress σ_{Nmin} as at least equal to -100 kPa, when the cohesion c is equal to 40 kPa (i.e., for the scale $l = 1$ m). From these observations, we deduce the following relationships, $\sigma_{Nmax} = \frac{5}{4}c$ and $\sigma_{Nmin} = -\frac{5}{2}c$, that are used to define the upper and lower limits on the normal stress. It should be noted that in the data analyzed by Weiss et al. (2007), highly biaxial compression stress states are absent, meaning that σ_{Nmin} could actually be much lower. We verified that using lower values for σ_{Nmin} does not significantly impact the results presented in this paper. However, in longer simulations, it may affect the spatial distribution of the sea ice thickness, for example, when the ice is constantly pushed towards the coast. Comparing simulated sea ice thickness fields to observations could help up to better determine the value of σ_{Nmin} to be used in the model.

2.2.3. Internal stress and damage evolution

In nature, the formation of a network of faults within a continuous sea ice cover is associated with avalanches of local damage events that propagates through the ice at the speed of the elastic waves. To reproduce this very rapid propagation process, the model presented in Girard et al. (2011) used a sub-iteration loop within each time step and a constant damage factor d_0. In our model we do not use sub-iteration and the damage factor Ψ is variable. The two approaches ensure that the internal stress is within a failure envelope at each time step. In our case the damage is still propagated but at a speed limited by the ratio $\frac{\Delta x}{\Delta t}$. For example at a resolution of 10 km and with a model time step of 800 s, it means that the damage could propagate in 3 days (i.e., the typical time scale at which sea ice motion is estimated from SAR-images) over 3240 km, i.e. about the size of the Arctic basin. To not use sub-iterations has no significant impact on the simulated sea ice deformation fields but has the advantage of reducing significantly the computational time.

In our model, the evolution of the damage is controlled by two terms, a damaging term (source) and a relaxation term (sink) corresponding to the recovery of the ice mechanical strength (i.e., healing). The evolution equation for the damage is written as:

$$\frac{Dd}{Dt} = \frac{\Delta d}{\Delta t} - \frac{d}{T_d}, \tag{16}$$

where Δd is the damage source term, which is defined hereafter, and T_d is the damage relaxation time, which is supposed to be much larger than the model time step Δt.

To obtain the evolution equation for the internal stress, we compute the time derivative of equation 7. By assuming that the healing and the variation of the concentration do not influence the internal stress but only the elastic stiffness, we get the following equation:

$$\frac{D\boldsymbol{\sigma}}{Dt} = \frac{\Delta d}{\Delta t}\frac{\partial \boldsymbol{C}}{\partial d} : \boldsymbol{\epsilon} + \boldsymbol{C}(A, d) : \dot{\boldsymbol{\epsilon}}, \tag{17}$$

where the deformation rate tensor is defined by $\dot{\boldsymbol{\epsilon}} = \frac{1}{2}\left(\nabla \boldsymbol{u} + (\nabla \boldsymbol{u})^T\right)$. The evolution of the internal stress is computed in two steps that would correspond to:

$$\frac{D\boldsymbol{\sigma}}{Dt} = \frac{\boldsymbol{\sigma}^{n+1} - \boldsymbol{\sigma}'}{\Delta t} + \frac{\boldsymbol{\sigma}' - \boldsymbol{\sigma}^n}{\Delta t}. \tag{18}$$

A first estimate of the internal stress, $\boldsymbol{\sigma}'$, is computed without considering the damaging process:

$$\frac{\boldsymbol{\sigma}' - \boldsymbol{\sigma}^n}{\Delta t} = \boldsymbol{C}(A^n, d^n) : \dot{\boldsymbol{\epsilon}}. \tag{19}$$

With this estimate, the failure criteria are checked. For the elements for which the estimated internal stress $\boldsymbol{\sigma}'$ falls outside the failure envelope, the damage factor Ψ is set to the value for which the stress state

$$\boldsymbol{\sigma}^{n+1} = \Psi \boldsymbol{\sigma}', \tag{20}$$

is set back on the failure envelope following the line crossing the origin of the normal and shear stress space. For the elements for which the estimated internal stress $\boldsymbol{\sigma}'$ is inside the failure envelope, Ψ is simply set to 1.

To obtain the damage source term Δd of equation 16, we rewrite the damage step (equation 20) as an evolution equation :

$$\frac{\boldsymbol{\sigma}^{n+1} - \boldsymbol{\sigma}'}{\Delta t} = \frac{(\Psi - 1)}{\Delta t} \boldsymbol{\sigma}'. \tag{21}$$

As the left hand side of equation 21 corresponds to the first term on the right hand side of equation 18, we deduce that the right hand side of equation 21 corresponds to the first term on the right hand side of equation 17:

$$\frac{\Delta d}{\Delta t} \frac{\partial \boldsymbol{C}}{\partial d} : \boldsymbol{\epsilon} = \frac{(\Psi - 1)}{\Delta t} \boldsymbol{\sigma}'. \tag{22}$$

We then derive the following expression

$$\frac{\partial \boldsymbol{C}}{\partial d} : \boldsymbol{\epsilon} = -\frac{1}{(1-d)}\boldsymbol{\sigma}, \tag{23}$$

by using the equivalence between equations 6 and 7 and the fact that $\frac{\partial E(A,d)}{\partial d} = -Yf(A) = -\frac{1}{(1-d)}E(A,d)$. Equation 23 is introduced in equation 22 and the terms are rearranged to finally obtain the equation for the damage source term

$$\Delta d = (1-\Psi)(1-d^n). \tag{24}$$

The variation of the damage has exactly the same form as in Girard et al. (2011), except that in our case the damage factor is not a constant chosen empirically but is computed locally to bring the internal stresses back onto the failure envelope in one time step. The increase of the damage induces a decrease of the effective elastic stiffness. The damaged sea ice deforming more easily, this may trigger new damaging events in the surrounding cells.

3. Implementation

The rheology generates discontinuities in the simulated fields at the scale of the elements (e.g., highly localized deformation). This constrains many aspects of the implementation of the model. This section describes the temporal and spatial discretizations of the equations, as well as the Lagrangian advection scheme, which is preferred to classical Eulerian schemes for its natural ability at transporting highly heterogeneous fields without modifying their spatial properties.

3.1. Temporal discretization

The first step consists in solving together the evolution equations for $\boldsymbol{u}$ and $\boldsymbol{\sigma}$. In Girard et al. (2011), the quasi-static assumption implied that no time evolution term was present in the momentum and the internal stress equations. In our case, both equations have a time derivative and are coupled together via the elastic term. To avoid the stability constrain due to elastic waves, the momentum and internal stress evolution equations are solved together with an implicit scheme as follows:

$$\begin{aligned}
\rho_i h^n \frac{\boldsymbol{u}^{n+1} - \boldsymbol{u}^n}{\Delta t} =& \nabla \cdot (h^n \boldsymbol{\sigma}') \\
&+ A^n \rho_a c_a \left|\boldsymbol{u}_a\right|_e (\boldsymbol{u}_a \cos\theta_a + \boldsymbol{k} \times \boldsymbol{u}_a \sin\theta_a) \\
&+ A^n \rho_w c_w \left|\boldsymbol{u}_w - \boldsymbol{u}^n\right|_e \left(\boldsymbol{u}_w - \boldsymbol{u}^{n+1}\right) \cos\theta_w \\
&+ A^n \rho_w c_w \left|\boldsymbol{u}_w - \boldsymbol{u}^n\right|_e \boldsymbol{k} \times (\boldsymbol{u}_w - \boldsymbol{u}^n) \sin\theta_w \\
&- \rho_i h^n \left(f\boldsymbol{k} \times \boldsymbol{u}^* + g\nabla\eta\right),
\end{aligned} \tag{25}$$

and

$$\frac{\boldsymbol{\sigma}' - \boldsymbol{\sigma}^n}{\Delta t} = \boldsymbol{C}(A^n, d^n) : \frac{1}{2}\left(\nabla \boldsymbol{u}^{n+1} + (\nabla \boldsymbol{u}^{n+1})^T\right). \tag{26}$$

Note that the symmetric part of the ocean drag term is treated implicitly, whereas the anti-symmetric part is treated explicitly to preserve the symmetry of the system that we need to solve. The Coriolis term is also treated explicitly to preserve the symmetry of the system. The operator $\left|\boldsymbol{u}\right|_e$ gives the norm of vector $\boldsymbol{u}$ over an element. The sea ice velocity $\boldsymbol{u}^*$ used in the

Coriolis term is defined as:

$$\boldsymbol{u}^* = \beta_0 \boldsymbol{u}^n + \beta_1 \boldsymbol{u}^{n-1} + \beta_2 \boldsymbol{u}^{n-2}, \tag{27}$$

where β_0, β_1 and β_2 are the coefficients of the third order Adams-Bashfort scheme (23/12, -16/12, 5/12), which is chosen for its stability (see Walters et al. (2009) for a stability analysis of time-stepping methods for the Coriolis term in a shallow water model). Using lower order schemes could be sufficient in the case of sea ice but it has not been investigated in the present study. For the first and second time steps, the coefficients are those of the first order (1, 0, 0) and second order (3/2, -1/2, 0) Adams-Bashfort schemes, respectively.

The second step consists in verifying the failure criteria and in computing for each element the damage factor Ψ as explained in Section 2.2.3. The new internal stress $\boldsymbol{\sigma}^{n+1}$ and damage d' are then given by:

$$\boldsymbol{\sigma}^{n+1} = \Psi \boldsymbol{\sigma}', \tag{28}$$

$$(d' - d^n) = (1 - \Psi)(1 - d^n). \tag{29}$$

The third step consists in updating the damage due to healing:

$$\frac{d^{n+1} - d'}{\Delta t} = -\frac{d'}{T_d}, \tag{30}$$

and the last step of the time stepping procedure consists in performing the advection of the different quantities.

3.2. Spatial discretization

The sea ice thickness, concentration and damage are defined as scalars at the center of each triangle, whereas the velocity fields are piecewise linear with nodal values defined at triangle vertices. The internal stress tensor, whose evolution is a function of the sea ice velocity gradient, is constant within each triangle.

The spatial discretization of the momentum equation is not trivial since it is strongly coupled to the evolution of the internal stress. Now that the temporal discretization is defined, we can regroup the terms depending on $\boldsymbol{u}^{n+1}$, the one depending on $\boldsymbol{\sigma}'$, and the rest, so that solving the momentum equation consists in finding the solution $\boldsymbol{u}^{n+1}$ of this problem:

$$k\boldsymbol{u}^{n+1} + \nabla \cdot (h^n \boldsymbol{\sigma}') + \boldsymbol{f} = 0, \qquad \forall \boldsymbol{x} \in \Omega, \tag{31}$$

with $\boldsymbol{u}^{n+1} = 0$ on the closed boundaries and $\boldsymbol{n} \cdot (h^n \boldsymbol{\sigma}') = 0$ on the open boundaries. $\boldsymbol{n}$ is the outward pointing normal on the open boundary. k is a scalar function that does not depend on $\boldsymbol{u}^{n+1}$. $\boldsymbol{f}$ is a vector regrouping all the terms that do not depend on $\boldsymbol{u}^{n+1}$ and $\boldsymbol{\sigma}'$. Hereafter $\boldsymbol{u}^{n+1}$ is simply noted $\boldsymbol{u}$ and equation 26 is used to replace $\boldsymbol{\sigma}'$ by a linear combination of $\boldsymbol{\sigma}^n$ and the new deformation rate tensor, which is denoted by the function $\boldsymbol{\epsilon}(\boldsymbol{u})$.

The discretization of this problem is performed by following the classical methodology of the finite element method (see for example Hughes (2012) for a reference textbook), which is composed of two steps: the definition of the variational (or weak) formulation of the problem and the approximation of the solution in a functional space that can be entirely defined with a finite number of unknowns.

In the present case, the equivalent variational form is to find $\boldsymbol{u}$ so that

$$\langle \hat{\boldsymbol{u}} \cdot (k\boldsymbol{u} + \nabla \cdot (h^n (\boldsymbol{\sigma}^n + \Delta t \boldsymbol{C} : \boldsymbol{\epsilon}(\boldsymbol{u}))) + \boldsymbol{f}) \rangle = 0, \qquad \forall \hat{\boldsymbol{u}} \in \mathcal{U}, \tag{32}$$

where the bracket $\langle \; \rangle$ refers to the integral over the domain, $\hat{\boldsymbol{u}}$ are the test functions and $\mathcal{U}$ is the functional space, which is here restricted to functions that cancel on closed boundaries.

By applying an integration by parts, the divergence theorem and the boundary conditions, we get:

$$k \langle \hat{\boldsymbol{u}} \cdot \boldsymbol{u} \rangle - h^n \langle (\nabla \hat{\boldsymbol{u}}) : \boldsymbol{\sigma}^n \rangle - h^n \Delta t \langle (\nabla \hat{\boldsymbol{u}}) : \boldsymbol{C} : \boldsymbol{\epsilon}(\boldsymbol{u}) \rangle + \langle \hat{\boldsymbol{u}} \cdot \boldsymbol{f} \rangle = 0, \quad \forall \hat{\boldsymbol{u}} \in \mathcal{U}. \tag{33}$$

After introducing $\boldsymbol{\epsilon}(\hat{\boldsymbol{u}})$, using the fact that $\frac{1}{2}\left(\nabla \hat{\boldsymbol{u}} - \nabla \hat{\boldsymbol{u}}^T\right) : \boldsymbol{C} : \boldsymbol{\epsilon}(\boldsymbol{u}) = 0$ as it is a product of an anti-symmetric and a symmetric tensor, and regrouping the unknowns on the left hand side, we get

$$k \langle \hat{\boldsymbol{u}} \cdot \boldsymbol{u} \rangle - h^n \Delta t \langle \boldsymbol{\epsilon}(\hat{\boldsymbol{u}}) : \boldsymbol{C} : \boldsymbol{\epsilon}(\boldsymbol{u}) \rangle = h^n \langle (\nabla \hat{\boldsymbol{u}}) : \boldsymbol{\sigma}^n \rangle - \langle \hat{\boldsymbol{u}} \cdot \boldsymbol{f} \rangle, \quad \forall \hat{\boldsymbol{u}} \in \mathcal{U}. \tag{34}$$

Following the finite element method, an approximate solution $\boldsymbol{u}^h$ is build as a linear combination of shape functions $\theta_j(\boldsymbol{x})$:

$$\boldsymbol{u}^h = \sum_{j=1}^{m} \mathbf{U}_j \theta_j(\boldsymbol{x}), \tag{35}$$

where $\mathbf{U}_j$ are the coefficients (i.e., nodal values) for the basis function $\theta_j(\boldsymbol{x})$ and m is the number of nodes. In our case, $\theta_j(\boldsymbol{x})$ are piecewise linear shape functions defining the discrete sub-space $\mathcal{U}^h \subset \mathcal{U}$. $\boldsymbol{f}^h$, the approximation of $\boldsymbol{f}$, is built in the same way as $\boldsymbol{u}^h$ with $\mathbf{F}_j$ as nodal values.

As all possible approximated solutions $\boldsymbol{u}^h$ and approximated test functions $\hat{\boldsymbol{u}}^h$ are built as linear combinations of the elements of the following base:

$$\left\{ \begin{bmatrix} \theta_1 \\ 0 \end{bmatrix}, \begin{bmatrix} 0 \\ \theta_1 \end{bmatrix}, \cdots, \begin{bmatrix} \theta_m \\ 0 \end{bmatrix}, \begin{bmatrix} 0 \\ \theta_m \end{bmatrix} \right\}, \tag{36}$$

solving the discrete problem is equivalent to solving the linear system:

$$\sum_{j=1}^{m} \mathbf{A}_{ij} \mathbf{U}_j = \mathbf{B}_j \qquad\qquad i = 1, \cdots, m, \tag{37}$$

where $\mathbf{A}_{ij}$ and $\mathbf{B}_i$ are assembled by summing the contributions of each element to the integral over the domain as explained in the Appendix. The system is currently solved with CHOLMOD, which is based on supernodal sparse Cholesky factorization (Chen et al., 2008).

It should be noted that the finite element method does not require to define shape functions $\theta_j(\boldsymbol{x})$ in a unique global coordinate system. One can define a nodal coordinates system to avoid pole singularities and to solve the equations on any smooth surface as in Comblen et al. (2009). This approach is however not yet implemented in our model, and so we use for this study a polar stereographic projection to define the spatial coordinates $\boldsymbol{x} = (x, y)$.

3.3. Advection scheme

Most sea ice models use an Eulerian approach for the advection. However, we believe that a purely Lagrangian approach as in Wang and Ikeda (2004) may be more appropriate. Purely Lagrangian schemes necessitate unstructured meshes and a procedure for the mesh adaptation. Nowadays, efficient libraries based on local mesh adaptation are available (see for example BAMG, `http://www.ann.jussieu.fr/hecht/ftp/bamg/bamg.pdf` or MAdLib, `http://http://sites.uclouvain.be/madlib/`). Local mesh modifications can be done in parallel and introduce very low numerical dissipation (Compère et al., 2009). It also verifies local conservation (Compère et al., 2008).

In the purely Lagrangian approach, the vertices of the element (i.e., the nodes of the grid) move with the sea ice velocity $\boldsymbol{u}$. The material derivative is then simply equal to the temporal derivative $\frac{\partial \phi}{\partial t}\Big|_X$ relative to the moving mesh so that the quantities are naturally transported with the ice. The sea ice thickness and concentration are simply updated by:

$$h^{n+1} = h^n \frac{S^n}{S^{n+1}}, \tag{38}$$

and

$$A^{n+1} = \min\left(A^n \frac{S^n}{S^{n+1}}, 1 \right), \tag{39}$$

where S^n and S^{n+1} are the surface of the element at time steps n and $n+1$.

In the Eulerian approach, the mesh is fixed and the transport of the different quantities from one cell to the others is computed by specific advection schemes. High-order advection schemes have been widely developed for structured meshes (e.g. Prather, 1986). When using the finite element method in the Eulerian approach, the choice of the advection scheme depends on the order of the spatial discretization. In our case, the quantities to be transported are represented by a scalar for each element. We could either choose an upwind scheme, which is highly diffusive or a centred scheme, which generates unrealistic oscillations (Hanert et al., 2004).

To illustrate the problem of numerical diffusion, we show an example when using an upwind Eulerian advection scheme for h and A. In this Eulerian approach, the mesh is fixed and the material derivative is defined as

$$\frac{D\phi}{Dt} = \left.\frac{\partial \phi}{\partial t}\right|_x + \boldsymbol{u} \cdot (\nabla \phi)\,, \tag{40}$$

where $\left.\frac{\partial \phi}{\partial t}\right|_x$ is the temporal derivative of the variable relative to a fixed referential. The sea ice thickness and concentration evolution within each element are computed by the budget of the upwind fluxes though its boundaries:

$$\frac{(h^{n+1} - h^n)}{\Delta t} = \frac{1}{S} \sum_{b=1}^{3} h_b^n \left(\boldsymbol{u}_b^{n+1} \cdot \boldsymbol{n}_b\right) L_b, \tag{41}$$

and

$$\frac{(A^{n+1} - A^n)}{\Delta t} = \frac{1}{S} \sum_{b=1}^{3} A_b^n \left(\boldsymbol{u}_b^{n+1} \cdot \boldsymbol{n}_b\right) L_b, \tag{42}$$

where L_b and $\boldsymbol{n}_b$ correspond to the length and the outward normal of the edge b, $\boldsymbol{u}_b$ is the sea ice velocity vector evaluated at the middle of the edge and h_b^n and A_b^n are the upwind sea ice thickness and concentration, respectively.

4. Sensitivity analysis

To analyze the sensitivity of the model, an Arctic configuration is set up on a triangular mesh having a mean resolution $\Delta x = 7$ km (i.e., each triangle of the mesh has a surface S of about 50 km^2). We use a polar stereographic projection centred on the North Pole and with the negative y-axis aligned with the 45W meridian. The domain extends from Bering Strait to Denmark Strait and to the shortest line linking Iceland and Norway across the Norwegian Sea. The northern gates of the Canadian Arctic Archipelago are closed, except Nares Strait. The coasts are defined at the resolution Δx by a B-spline interpolation of a coarsened set of the Global Self-consistent, Hierarchical, High-resolution Shoreline database (GSHHS) following the method explained by Lambrechts et al. (2008). All these operations are performed with the Gmsh mesh generator (Geuzaine and Remacle, 2009). The boundary conditions are no slip everywhere except at the open boundaries (Nares Strait, Bering Strait, Denmark Strait and in the Norwegian Sea) that have a zero stress condition.

A consequence of using a Lagrangian advection scheme is that a remeshing scheme is needed to adapt the mesh when it becomes too distorted. The use of a remeshing scheme is not necessary here since the simulations we performed are relatively short (i.e. 10 days). Over such period of time the deformation of the mesh is not generating badly shaped triangles that require a remeshing procedure. In addition of not calling any remeshing method, the forcings and the shape coefficients used for the spatial discretization are defined relative to the initial position of the mesh. This approach is only valid for short simulations though (a few days) as it progressively introduces errors in the position of the ice relative to the geometry and the forcing. On time scales of few days the mechanical recovery due to the healing of the sea ice is supposed to be negligible. The healing term is therefore deactivated in the simulations we present here by setting the damage relaxation time to a very large value ($T_d = 10^{20}$ seconds).

The atmospheric forcing fields consist in the 3-hourly 10-meter wind velocities coming from the Arctic System Reanalysis (ASR) distributed at 30 km spatial resolution (`http://rda.ucar.edu/datasets/ds631.0/`, Byrd Polar Research Center/The Ohio State University (2012). Accessed 01 Jan 2014). The oceanic forcing fields consist in the daily elevation and 30-meter depth velocities of the ocean coming from the TOPAZ reanalysis at an average spatial resolution of 12.5 km in the Arctic (Sakov et al., 2012). The simulations presented hereafter all ran over the same 10-day period, 5-15 March 2008. The forcings are progressively applied during a spin-up period of one day.

To keep the presentation of this model concise, we follow the classical formulation where the values for the turning angles and drag coefficients are constant in time and over the whole domain. This approach is an approximation that does not reflect the status of the knowledge concerning the boundary layers above and below the ice (McPhee, 2012) and the recent efforts to build new parameterizations of the drag (Tsamados et al., 2014). The water turning angle is fixed at 25°, which is a common value for sea ice (Leppäranta, 2005), whereas there is no turning angle applied to the surface wind stress computed from ASR wind velocities. The values of the drag coefficients c_a and c_w, and more specifically the ratio between the two, may depend on the forcing and could be tuned along with other parameters to improve the simulations made with a given model. Different tuning experiments have led to different optimized ratio for the Arctic. Massonnet et al.

(2014) estimated that the optimal value for c_a/c_w was equal to 0.48 for the NEMO-LIM3 model forced by NCEP/NCAR winds (analyzed period: winter seasons 2007 and 2012). Kreyscher and Flato (2000) found $c_a/c_w = 0.5$ for the VP model forced by ECMWF winds (analyzed period: 1979-1994). Miller et al. (2006) found for the CICE sea ice model forced by ECMWF (ERA-40) winds different ratios ranging from 0.11 to 0.3 (analyzed period: 1994-2001). All these analysis compared the simulated and observed sea ice drift over the whole Arctic basin, leading to interdependence between the optimization of the mechanical parameters and the optimization of the drag coefficients. We here propose a tuning approach that has the advantage to differentiate the choice of the drag coefficients from the mechanical parameters. Instead of tuning the drag coefficients over the whole domain, we select a region South of Fram Strait, where sea ice generally moves in a free drift mode. For this region, we tuned the air and water drag coefficients by comparing the simulated and SAR-derived sea ice velocities over the period 18-28 Feb 2008. From the following pairs of c_a, c_w=[0.003,0.003; 0.003,0.004; 0.003,0.0055; 0.004,0.004; 0.004,0.0055], we found that the lowest error (defined in terms of the norm of the difference between the simulated and observed velocity vector) is obtained with $c_a = 0.003$ and $c_w = 0.004$. Here, the value used for c_a/c_w is found to be higher than the classical values. This is consistent with the fact that ASR surface winds are weaker than the geostrophic winds and than the surface wind of ERA-INTERIM produced by ECMWF (Bromwich et al., 2015), which are frequently used to force large scale sea ice models.

In the following cases, the initial sea ice damage, velocities and internal stresses are set to zero. For the sea ice concentration, two different initial conditions are used: either the sea ice concentration A_{topaz} from the TOPAZ reanalysis or the sea ice concentration A_{obs} from observations. A_{obs} is defined as a combination of the sea ice concentration and lead area fraction fields coming respectively from two different datasets: the AMSR-E/ASI sea ice concentration, here denoted A_{tot} (http://www.iup.uni-bremen.de/seaice/amsr/, University of Bremen, Bremen, Germany, October 2011) and the AMSR-E lead area fraction, here denoted A_{lead} (http://icdc.zmaw.de/, Integrated Climate Date Center, University of Hamburg, Hamburg, Germany, May 2014). Both datasets are given at 6.5km horizontal resolution (see Spreen et al. (2008) and Röhrs and Kaleschke (2012) for the description of the methodologies). A_{lead} and A_{tot} provide different information. A_{lead} identifies the narrow leads in high concentration areas from anomalies in the brightness temperature ratio whereas A_{tot} provides the smooth background concentration fields and may also identify large open water areas such as polynias. To study the impact of having information on the leads in the initial condition, we define the ice concentration A_{obs} as:

$$A_{obs} = A_{tot} \left(1 - A_{lead}\right), \tag{43}$$

The two sets of initial conditions, A_{topaz} and A_{obs}, are very similar in term of sea ice extent but differ significantly in terms of sea ice concentration distribution (not shown here) because of the representation of the leads. A_{topaz} is relatively smooth, whereas A_{obs} already contains localized linear features (Figure 1). From the mechanical point of view, initialization with A_{obs} is preferred as the ice in the leads is generally the weakest, which in turn potentially impacts the results of the simulation. The impact of starting from one dataset or the other is analyzed in section 4.3. For the sea ice thickness, two different initial conditions are also defined. When A_{topaz} is used, the initial sea ice thickness h_{topaz} is directly taken from the TOPAZ reanalysis. When A_{obs} is used, the initial sea ice thickness h_{obs} is also derived from the TOPAZ reanalysis but is corrected to be consistent with A_{obs} by defining h_{obs} as:

$$h_{obs} = \frac{h_{topaz}}{A_{topaz}} A_{obs}, \tag{44}$$

The reference simulation runs with the Lagrangian scheme, is initialized with A_{topaz} and h_{topaz} and uses the following set of parameters: $c = 4$ kPa, α=-20, $\Delta t = 800$ s and $Y = 9$ GPa. Simulations with smaller time steps (Δt set to 100, 200 and 400 s) produce similar results than the one with $\Delta t = 800$ s but simulations with larger time steps (Δt set to 2400, 7200 and 21600 s) do not, presumably because the time step is not small enough compared to the forcing time scale.

The sea ice velocity fields, simulated over the last 3 days of the 10-day simulations, exhibit spatial discontinuities, which are located along quasi linear features spanning almost the entire Arctic basin (Figure 2, for the reference simulation). In the following sections, we discuss the realism of the simulated dynamics by analysing the deformation fields and we present the sensitivity of the model to the type of advection scheme, to the initial conditions and to the value of the cohesion parameter c and compactness parameter α. The sensitivity to Y has been discussed in section 2.

4.1. Sensitivity to the advection scheme

To preserve discontinuities in the ice concentration and thickness fields when sea ice moves requires a particular attention to the choice of the advection scheme. Starting from the same initial conditions, A_{obs} and h_{obs}, and with the same forcing fields and parameters, the simulations with the Lagrangian scheme and the Eulerian upwind scheme give radically different sea ice concentration and thickness fields after a period as short as 10 days (Figure 3). With the Lagrangian scheme, the distribution of sea ice concentration remains similar to the observations, whereas the distribution obtained for the Eulerian upwind scheme is greatly affected by numerical diffusion. However, one should note that Eulerian upwind schemes are known to be much more diffusive than other Eulerian schemes. This example is only presented as an illustration and is meant to show that the Lagrangian approach at least can naturally conserve discontinuities even when they are located at the native resolution of the model.

4.2. Statistical analysis of the simulated sea ice deformation

The simulated ice deformation fields shown in Figure 4 (i.e. shear and divergence) exhibit obvious localization properties expressed by the presence of linear features (the so-called linear kinematics features, Kwok (2000)). However, to evaluate the realism of the deformation fields requires a thorough statistical analysis. We performed such analysis using the deformation derived from the sea ice displacement field simulated over the last 3 days of 10-day simulations and on a domain restricted to the elements of the Arctic basin being at least 150 km away from the coast. Several statistical diagnostics are used for the analysis, i.e. the cumulative distribution of sea ice deformation, the total shearing, opening and closing rates, and the characteristics of the spatial scaling of sea ice deformation. These diagnostics can be computed for SAR-derived drift and deformation datasets, and compared to the values obtained with the model. Such comparison has been routinely done during the development of the present model for a large set of simulations, and showed very good agreement. These results will be presented in a dedicated paper.

The cumulative distributions (i.e., the probability of exceedance) for the shear and divergence rates are computed as in Marsan et al. (2004) and are plotted in semi-log scale to highlight the differences between the simulations (Figure 4). The same results plotted in logarithmic scales (not shown here) show similar power law tails as in Marsan et al. (2004). One should note that detection and characterization of power law tails in statistical distributions are very sensitive to the method of analysis and therefore require a proper quality check (Clauset et al., 2009).

The total opening $< \dot{\mathcal{O}} >$, closing $< \dot{\mathcal{C}} >$ and shearing $< \dot{\mathcal{S}} >$ rates are computed by integrating over the domain of analysis the positive divergence, negative divergence and shear rates respectively (Table 3). For the reference simulation the total opening rate $< \dot{\mathcal{O}} >$ is equal to 15000 km^{2}day^{-1} and the total closing rate $< \dot{\mathcal{C}} >$ is equal to -24000 km^{2}day^{-1}. These quantities are more interesting than the total divergence rate as they are related to the opening and closing of leads and to the formation of ridges. These integrated values but also the ratio between opening and closing vary drastically at the typical time scale of the wind forcing and should be analyzed in a statistical sense over a month or a season, and not just from one snapshot.

However, snapshot analyses remain useful for estimating the sensitivity to model parameters (see the following subsections).

The heterogeneity of the deformation fields is estimated by computing the area that accommodates the largest 50% of the deformation as in Girard et al. (2011). $\delta_{\dot{\mathcal{O}}_{50\%}}$, $\delta_{\dot{\mathcal{C}}_{50\%}}$ and $\delta_{\dot{\mathcal{S}}_{50\%}}$ are defined as the minimum fractions of the total area needed to accommodate 50% of the total opening, closing and shearing rate, respectively (see Stern and Lindsay (2009) for a more complete description of the method). A homogeneous deformation field would give $\delta_{\dot{\mathcal{S}}_{50\%}} = 50\%$. The deformation fields simulated by our model are highly heterogeneous. For the reference simulation, 50% of the largest shear are accommodated by only 8% of the domain area. In Girard et al. (2011), $\delta_{\dot{\mathcal{S}}_{50\%}}$ was equal to 4% for a simulation with the EB rheology and to 6% for observations (model and observations being at the same resolution of 10 km and computed for the same date). The value of these diagnostics for the different simulations are given in Table 3.

The spatial scaling of the deformation is determined as in Marsan et al. (2004). A coarse-graining procedure is performed to compute the shear and divergence rate fields at different spatial scales L (Figure 5). The spatial scaling of the total deformation is similar to the one of the shear and is not presented here. The mean of the distribution (i.e., first order moment) of the simulated shear and absolute divergence rates computed at different scales can be described by a power law:

$$< \dot{\epsilon} >_L \sim L^{-\beta(1)}, \tag{45}$$

with different scaling exponent $\beta_{shear}(1)$ and $\beta_{div}(1)$ (Table 4). For the reference simulation, we found $\beta_{shear}(1) = 0.04$ and $\beta_{div}(1) = 0.15$. Previous studies have analysed the scaling properties of sea ice deformation. Stern and Lindsay (2009), for example, found a mean scaling exponent of 0.18 with a standard deviation of 0.10 for the total deformation computed from satellite-derived observations covering several winter seasons. However, as shown in Bouillon and Rampal (2014), the artificial noise present in the deformation dataset used for these studies could lead to an overestimation of these spatial scaling exponents of about 60% for the shear and total deformation, and 100% for the absolute divergence. Moreover, due to the high variability in time of these exponents, one should not compare the values obtained over a unique example but rather the distributions of the simulated and observed scaling exponents over a season.

How the distribution of the deformation varies with the scale of computation can be fully described by performing a multifractal analysis, which consists in looking at the different moment orders q of the distribution. Similarly to observed sea ice deformation fields, model data follow the power law scaling $< \dot{\epsilon}^q >_L \sim L^{-\beta(q)}$ with $\beta(q)$ being a quadratic function of $0 \leq q \leq 3$. The structure function $\beta(q)$ (Figure 6) characterizes how the moments of the distribution evolve as a function of the spatial scale (i.e., $\beta(1)$ for the mean, $\beta(2)$ for the standard deviation, $\beta(3)$ for the skewness). The curvature of the structure functions $\beta(q)$ indicates that our simulated sea ice deformation fields show a multifractal spatial scaling. The curvature is described by the coefficient a of the quadratic fit $\beta(q) = aq^2 + bq$, and its value gives the degree of multifractality of the scaling. For the reference simulation, we found $a_{shear} = 0.18$ and $a_{div} = 0.23$. For comparison, Marsan et al. (2004) found

$a = 0.13$ for a total deformation field derived from observations. The values of this diagnostic for the different simulations are recapped in Table 4.

4.3. Sensitivity to the initial conditions

To study the impact of the initial conditions, a simulation is started with A_{obs} and h_{obs} and compared to the reference simulation. We found similar distributions of deformation (Figure 4), and almost identical values for the total opening, closing and shearing rate (16 000, -25 000, 103 000 km^{2}day^{-1}, respectively) and for $\delta_{\dot{\mathcal{O}}_{50\%}}$, $\delta_{\dot{\mathcal{C}}_{50\%}}$ and $\delta_{\dot{\mathcal{S}}_{50\%}}$ (0.06, 0.005, 0.08, respectively). The structure function $\beta(q)$ is also very close to the one obtained for the reference simulation (Figure 6). The only significant difference concerns the bars on $\beta(q)$ function that quantifies the deviation from the power law scaling (see caption of Figure 6 for more details). These are larger compared to the reference run, especially for the absolute divergence rate. In both cases, results exhibit a strong spatial localization and similar statistical properties, meaning that this characteristic of the model is not inherited from initial conditions but rather generated by the model itself. For the rest of the sensitivity study, we only use simulations initialized with A_{topaz} and h_{topaz} so that there are no discontinuities in the initial fields.

4.4. Sensitivity to the cohesion parameter c

Simulations with the cohesion parameter equal to 8, 4, 2, 1 and 0.5 kPa are performed and their results summarized in Tables 3 and 4 and in Figure 7. Decreasing the value of the cohesion parameter induces higher but less localized deformation (i.e., significant increase of the total opening $< \dot{\mathcal{O}} >$, closing $< \dot{\mathcal{C}} >$ and shearing $< \dot{\mathcal{S}} >$ rates and almost a doubling of $\delta_{\dot{\mathcal{O}}_{50\%}}$,

$\delta_{\dot{\mathcal{C}}_{50\%}}$ and $\delta_{\dot{\mathcal{S}}_{50\%}}$). Changing the value of the cohesion also changes the visual appearance of the deformation fields. For example, the simulation with c=0.5 kPa (Figure 7) shows many more features than in the reference simulation (Figure 4). For the shear rate distribution, decreasing the cohesion induces a gradual shift to higher values. For the divergence rate distribution, such a gradual shift is not observed, all the distributions are similar except for the simulation with c=8 kPa. The cohesion has also a clear impact on the structure functions $\beta(q)$ (Figure 7) as the curvatures a_{shear} and a_{div} decrease by almost a factor of 2 between the reference simulation (with c=4 kPa) and the simulation with the lowest cohesion (c=0.5 kPa)(Table 4). Overall we note that the cohesion parameter is the one having the highest impact on the degree of multifractality of the spatial scaling of the simulated deformation fields.

4.5. Sensitivity to the compactness parameter α

Simulations with the compactness parameter ranging -40, -20, -10 and 0 are performed (see Tables 5 and 6 and Figure 8). Increasing α from -40 to 0 leads to higher values for the effective elastic stiffness and then induces lower deformation, especially for the opening and closing rates. It also significantly decreases the heterogeneity of the shear deformation fields (i.e., increase of $\delta_{\dot{\mathcal{S}}_{50\%}}$) and induces lower scaling exponent (estimated by $\beta(1)$). However, it has only small impacts on the degree of multifractality (estimated by a). Moving α towards 0 leads to a more symmetrical distribution of divergence (Figure 8), whereas the distribution of the shear rate is almost unchanged. Symmetry of the distribution of divergence has been reported in Girard et al. (2009) and shown to depend on the spatial scale. This suggests that the best estimate of the compactness parameter for being used in our model could be established by performing a thorough comparison against observations.

5. Conclusions

The dynamical core of this new sea ice model neXtSIM is presented and outputs from 10-days sea ice standalone simulations are analyzed to evaluate the sensitivity of simulated sea ice dynamics to model parameters. neXtSIM is a Lagrangian model running on an unstructured finite element mesh. The introduction of the sea ice damage variable produces discontinuities at the scale of the elements in the simulated fields. We propose a specific implementation for the temporal and spatial discretization as well as for the advection scheme in order to preserve as much as possible these discontinuities over time. The model produces sea ice deformation fields showing similar statistical signatures as those found for the Arctic sea ice cover, and especially a multifractal spatial scaling invariance. These statistical properties do not rely on the realism of the initial concentration and thickness fields but rather emerge from the sea ice rheological model. The sensitivity analysis shows that the degree of multifractality of the sea ice deformation scaling invariance is mainly controlled by the cohesion parameter c. The compactness parameter α mainly impacts the total opening and closing rate with minor impact on the total shear rate. An extensive validation of the current model based on the comparison of the simulated fields against SAR-derived drift and deformation fields has been performed but will be presented in a dedicated study for more clarity. It would be important to evaluate the impact of using such sea ice model over longer time scales by looking at the seasonal cycle, spatial distribution and inter-annual variability of the sea ice concentration, thickness and velocities. However, further model developments are required to perform long simulations. First, sea ice thermodynamics has to be implemented and taken into account to parameterize the recovery of the ice mechanical strength (i.e. "healing") due to thermal forcing. Second, a remeshing procedure has to be implemented to adapt the mesh when it becomes too deformed. Finally, the coupling with an interacting ocean and atmosphere could also be necessary to asses the impact of better resolving sea ice dynamics on the other components of the Arctic system.

Appendix: Assembly of the finite element matrices

To compute the values of $\mathbf{A}_{ij}$ and $\mathbf{B}_i$, a transformation is applied to work in a parametric space defined by $\boldsymbol{\xi} = (\xi, \eta)$ instead of $\boldsymbol{x} = (x, y)$. All the elements are related to a unique parent element thanks to the transformation:

$$\boldsymbol{x}(\boldsymbol{\xi}) = \phi_1(\xi, \eta)\boldsymbol{X}_1^e + \phi_2(\xi, \eta)\boldsymbol{X}_2^e + \phi_3(\xi, \eta)\boldsymbol{X}_3^e, \tag{46}$$

where $\boldsymbol{X}_1^e$, $\boldsymbol{X}_2^e$ and $\boldsymbol{X}_3^e$ are the coordinates of the first, second and third vertices of the element e and

$$\begin{aligned}\phi_1(\xi, \eta) &= 1 - \xi - \eta, \\ \phi_2(\xi, \eta) &= \xi, \\ \phi_3(\xi, \eta) &= \eta.\end{aligned} \tag{47}$$

The sum over the nodes is then replaced by a sum over the three vertices of each element and $\boldsymbol{u}^h$ is then built as

$$\boldsymbol{u}^h = \sum_{i=1}^{3} \mathbf{U}_i^e \phi_i^e(\boldsymbol{x}), \tag{48}$$

where $\phi_j(\boldsymbol{x}) = \phi_j(\boldsymbol{\xi}(\boldsymbol{x}))$. The local base is then defined as:

$$\left\{ \begin{bmatrix} \phi_1^e \\ 0 \end{bmatrix}, \begin{bmatrix} 0 \\ \phi_1^e \end{bmatrix}, \begin{bmatrix} \phi_2^e \\ 0 \end{bmatrix}, \begin{bmatrix} 0 \\ \phi_2^e \end{bmatrix}, \begin{bmatrix} \phi_3^e \\ 0 \end{bmatrix}, \begin{bmatrix} 0 \\ \phi_3^e \end{bmatrix} \right\}. \tag{49}$$

With this representation, the values of the deformation rate tensor are then computed by

$$\boldsymbol{\epsilon}(\boldsymbol{u}) = \mathbf{G}^e\mathbf{U}^e, \tag{50}$$

where

$$\mathbf{U}^e = \begin{bmatrix} \mathrm{U}^e_{x1} \\ \mathrm{U}^e_{y1} \\ \mathrm{U}^e_{x2} \\ \mathrm{U}^e_{y2} \\ \mathrm{U}^e_{x3} \\ \mathrm{U}^e_{y3} \end{bmatrix}, \tag{51}$$

and

$$\mathbf{G}^e = \begin{bmatrix} \phi^e_{1,x} & 0 & \phi^e_{2,x} & 0 & \phi^e_{3,x} & 0 \\ 0 & \phi^e_{1,y} & 0 & \phi^e_{2,y} & 0 & \phi^e_{3,y} \\ \phi^e_{1,y} & \phi^e_{1,x} & \phi^e_{2,y} & \phi^e_{2,x} & \phi^e_{3,y} & \phi^e_{3,x} \end{bmatrix}. \tag{52}$$

The derivatives of the shape functions, also called shape coeficients, are computed by:

$$\begin{aligned} \phi^e_{1,x} &= (Y^e_2 - Y^e_3)/J^e, \quad \phi^e_{1,y} = (X^e_2 - X^e_3)/J^e, \\ \phi^e_{2,x} &= (Y^e_3 - Y^e_1)/J^e, \quad \phi^e_{2,y} = (X^e_3 - X^e_1)/J^e, \\ \phi^e_{3,x} &= (Y^e_1 - Y^e_2)/J^e, \quad \phi^e_{3,y} = (X^e_1 - X^e_2)/J^e, \end{aligned} \tag{53}$$

where J^e, the Jacobian of the transformation (i.e., $\det\left(\frac{\partial \boldsymbol{x}}{\partial \boldsymbol{\xi}}\right)$), is computed as

$$J^e = X_2^e Y_3^e + X_3^e Y_1^e + X_1^e Y_2^e - X_2^e Y_1^e - X_3^e Y_2^e - X_1^e Y_3^e. \tag{54}$$

The local contributions of $\mathbf{A}_{ij}$ and $\mathbf{B}_i$ are then given by:

$$\mathbf{A}_{ij}^e = k^e \mathbf{M}^e - h^e \Delta t \, \mathrm{S}^e \mathrm{E}^e \left(\mathbf{G}^e\right)^T \mathbf{D} \mathbf{G}^e, \tag{55}$$

and

$$\mathbf{B}_i^e = h^e \mathrm{S}^e \left(\mathbf{G}^e\right)^T \boldsymbol{\sigma}^e - \mathbf{M}^e \mathbf{F}^e, \tag{56}$$

where S^e is the surface of the element, which is actually equal to $J^e/2$. $\mathbf{M}^e$ is the local mass matrix, h^e is the value of h for the element e, E^e is the value of $E(A, d)$ for the element e, $\mathbf{F}^e$ contains the values of the vector $\boldsymbol{f}$ at the 3 nodes of the element e, and

$$\boldsymbol{\sigma}^e = \begin{bmatrix} \sigma_{11}^e \\ \sigma_{22}^e \\ \sigma_{12}^e \end{bmatrix}. \tag{57}$$

The local mass matrix is equal to:

$$\mathbf{M}^e = \begin{bmatrix} \langle\phi_1^e\phi_1^e\rangle & 0 & \langle\phi_1^e\phi_2^e\rangle & 0 & \langle\phi_1^e\phi_3^e\rangle & 0 \\ 0 & \langle\phi_1^e\phi_1^e\rangle & 0 & \langle\phi_1^e\phi_2^e\rangle & 0 & \langle\phi_1^e\phi_3^e\rangle \\ \langle\phi_2^e\phi_1^e\rangle & 0 & \langle\phi_2^e\phi_2^e\rangle & 0 & \langle\phi_2^e\phi_3^e\rangle & 0 \\ 0 & \langle\phi_2^e\phi_1^e\rangle & 0 & \langle\phi_2^e\phi_2^e\rangle & 0 & \langle\phi_2^e\phi_3^e\rangle \\ \langle\phi_1^e\phi_3^e\rangle & 0 & \langle\phi_3^e\phi_2^e\rangle & 0 & \langle\phi_3^e\phi_3^e\rangle & 0 \\ 0 & \langle\phi_3^e\phi_1^e\rangle & 0 & \langle\phi_3^e\phi_2^e\rangle & 0 & \langle\phi_3^e\phi_3^e\rangle \end{bmatrix}, \tag{58}$$

where $\left\langle\phi_i^e\phi_j^e\right\rangle = \frac{1}{12}\mathrm{S}^e$ when $i \neq j$ and $\left\langle\phi_i^e\phi_j^e\right\rangle = \frac{2}{12}\mathrm{S}^e$ when $i = j$.

Acknowledgements

Sylvain Bouillon is supported by the Research Council of Norway through the post-doc project SIMech, Sea Ice Mechanics: from satellites to numerical models (No. 231179/F20, 2014-2016). We would like to thank Total E&P for their support and the reviewers for their useful comments.

Amitrano, D., Grasso, J. R., Hantz, D., 1999. From diffuse to localised damage through elastic interaction. Geophys. Res. Lett. 26 (14), 2109–2112.

Bouillon, S., Rampal, P., 2014. On producing sea ice deformation dataset from sar-derived sea ice motion. The Cryosphere Discussions 8 (5), 5105–5135.
URL http://www.the-cryosphere-discuss.net/8/5105/2014/

Bower, A. F., 2011. Applied mechanics of solids. CRC press.
URL http://solidmechanics.org

Bromwich, D. H., Wilson, A. B., Bai, L.-S., Moore, G. W. K., Bauer, P., 2015. A comparison of the regional arctic system reanalysis and the global era-interim reanalysis for the arctic. Quarterly Journal of the Royal Meteorological Society, n/a–n/a.
URL http://dx.doi.org/10.1002/qj.2527

Chen, Y., Davis, Timothy, A., Hager, William, W., Rajamanickam, S., 2008. Algorithm 887: CHOLMOD, Supernodal Sparse Cholesky Factorization and Update/Downdate. ACM Transactions on Mathematical Software 35, 22:1–22–14.

Clauset, A., Shalizi, C., Newman, M., 2009. Power-law distributions in empirical data. SIAM Review 51 (4), 661–703.
URL http://dx.doi.org/10.1137/070710111

Comblen, R., Legrand, S., Deleersnijder, E., Legat, V., 2009. A finite element method for solving the shallow water equations on the sphere. Ocean Mod. 28, 12–23.

Compère, G., Remacle, J.-F., Jansson, J., Hoffman, J., 2009. A mesh adaptation framework for dealing with large deforming meshes. Int. J. Numer. Meth. Engng. 82, 843–867.

Compère, G., Remacle, J. F., Marchandise, E., 2008. Transient mesh adaptivity with large rigid-body displacements. In: Garimella, R. (Ed.), Proceedings of the 17th International Meshing Roundtable. Springer, Berlin, pp. 213–230.

Connolley, W. M., Gregory, J. M., Hunke, E. C., McLaren, A. J., 2004. On the consistent scaling of terms in the sea-ice dynamics equation. J. Phys. Oceanogr. 34, 1776–1780.

Geuzaine, C., Remacle, J.-F. c. o., 2009. Gmsh: a three-dimensional finite element mesh generator with buit-in pre- and post-processing facilities. International Journal For Numerical Methods In Engineering 79, 1309–1331.

Girard, L., Bouillon, S., Weiss, J., Amitrano, D., Fichefet, T., Legat, V., 2011. A new modelling framework for sea ice mechanics based on elasto-brittle rheology. Ann. Glaciol. 52(57), 123–132.

Girard, L., Weiss, J., Molines, J.-M., Barnier, B., Bouillon, S., Aug. 2009. Evaluation of high-resolution sea ice models on the basis of statistical and scaling properties of Arctic sea ice drift and deformation. J. Geophys. Res. 114 (C8).

Hanert, E., Le Roux, D. Y., Legat, V., Deleersnijder, E., 2004. Advection schemes for unstructured grid ocean modelling. Ocean Model. 7, 39–58.

Herman, A., 2013. Numerical modeling of force and contact networks in fragmented sea ice. Ann. Glaciol. 54 (62), 114–120.

Hibler, W. D., 1979. A dynamic thermodynamic sea ice model. J. Phys. Ocean. 9, 817–846.

Hughes, T. J. R., 2012. The Finite Element Method: Linear Static and Dynamic Finite Element Analysis. Dover Civil and Mechanical Engineering. Dover Publications.

Hunke, E. C., Dukowicz, J. K., 2003. The sea ice momentum equation in the free drift regime. Tech. rep., T-3 Fluid Dynamics Group, Los Alamos National Laboratory.

Hutchings, J. K., Heil, P., Hibler, W. D., 2005. Modeling linear kinematic features in sea ice. Month. Weath. Rev. 133 (12), 3481–3497.

Kreyscher, M., Flato, G. M., 2000. Results of the Sea Ice Model Intercomparison Project: Evaluation of sea ice rheology schemes for use in simulations Project (SIMIP). Four different sea ice theology schemes. Journal of Geophysical Research 105 (C5), 112299–11320.

Kwok, R., 2000. Deformation of the Arctic ocean sea ice cover between November 1996 and April 1997: A survey. IUTAM Symposium on Scaling Laws in Ice Mechanics and Ice Dynamics, 1–12.

Kwok, R., 2006. Contrasts in sea ice deformation and production in the Arctic seasonal and perennial ice zones. J. Geophys. Res. 111 (C11).

Lambrechts, J., Comblen, R., Legat, V., Geuzaine, C., Remacle, J. F., 2008. Multiscale mesh generation on the sphere. Ocean Dyn. 58 (5), 461–473.

Leppäranta, M., 2005. The Drift of Sea Ice. Springer, Helsinki.

Marcq, S., Weiss, J., 2012. Influence of sea ice lead-width distribution on turbulent heat transfer between the ocean and the atmosphere. The Cryosphere, Volume 6, Issue 1, 2012, pp. 143-156 6, 143–156.

Marsan, D., Stern, H. L., Lindsay, R., Weiss, J., Oct. 2004. Scale dependence and localization of the deformation of Arctic sea ice. Phys. Rev. Lett. 93 (17), 178501.

Marsan, D., Weiss, J., Aug. 2010. Space/time coupling in brittle deformation at geophysical scales. Earth Planet. Sci. Lett. 296 (3-4), 353–359.

Marsan, D., Weiss, J., Metaxian, J.-P., Grangeon, J., Roux, P.-F., Haapala, J., 2011. Low-frequency bursts of horizontally polarized waves in the Arctic sea-ice cover. J. Glaciol. 57 (202), 231–237.

Massonnet, F., Goosse, H., Fichefet, T., Counillon, F., 2014. Calibration of sea ice dynamic parameters in an ocean-sea ice model using an ensemble Kalman filter. Journal of Geophysical Research: Oceans 119 (7), 4168–4184.

McPhee, M. G., 2012. Advances in understanding ice-ocean stress during and since AIDJEX. Cold Regions Science and Technology 76-77, 24–36.

Mellor, M., 1986. Mechanical Behavior of Sea Ice. In: Untersteiner, N. (Ed.), The Geophysics of Sea Ice. NATO ASI Series. Springer US, Ch. 2, pp. 165–282.

Miller, P. A., Laxon, S. W., Feltham, D. L., 2006. Optimization of a sea ice model using basinwide observations of Arctic sea ice thickness, extent, and velocity. J. Climate 19, 1089–1108.

Morison, J. H., McPhee, M., 2001. Ice-ocean interaction.

Nukala, P. K. V. V., Zapperi, S., Simunovic, S., 2005. Statistical properties of fracture in a random spring model. Phys. Rev. E 71 (6), 066106.

Prather, M. J., 1986. Numerical advection by conservation of second-order moments. J. Geophys. Res. 91, 6671–6681.

Rampal, P., Weiss, J., Marsan, D., Bourgoin, M., Oct. 2009. Arctic sea ice velocity field: General circulation and turbulent-like fluctuations. J. Geophys. Res. 114 (C10), C10014.

Rampal, P., Weiss, J., Marsan, D., Lindsay, R., Stern, H. L., Dec. 2008. Scaling properties of sea ice deformation from buoy dispersion analysis. J. Geophys. Res. 113 (C3), C03002.

Richter-Menge, J. A., McNutt, S. L., Overland, J. E., Kwok, R., 2002. Relating Arctic pack ice stress and deformation under winter conditions. J. Geophys. Res. 107 (C10), 8040.

Röhrs, J., Kaleschke, L., 2012. An algorithm to detect sea ice leads by using AMSR-E passive microwave imagery. The Cryosphere 6 (2), 343–352.

Sakov, P., Counillon, F., Bertino, L., Lisæter, K. A., Oke, P., Korablev, A., 2012. TOPAZ4: An ocean sea ice data assimilation system for the North Atlantic and Arctic. Ocean Sci. 8, 633–662.

Schulson, E. M., 2004. Compressive shear faults within Arctic sea ice: Fracture on scales large and small. J. Geophys. Res. 109 (C7).

Schulson, E. M., 2009. Fracture of ice and other coulombic materials. Mechanics of Natural Solids, 177.

Schulson, E. M., Fortt, A. L., Iliescu, D., Renshaw, C. E., 2006. Failure envelope of first-year Arctic sea ice: The role of friction in compressive fracture. J. Geophys. Res. 111, C11S25.

Spreen, G., Kaleschke, L., Heygster, G., 2008. Sea ice remote sensing using AMSR-E 89-GHz channels. Journal of Geophysical Research: Oceans 113 (C2).

Stern, H. L., Lindsay, R., Oct. 2009. Spatial scaling of Arctic sea ice deformation. J. Geophys. Res. 114 (C10).

Sulsky, D., Schreyer, H., Peterson, K., Kwok, R., Coon, M., Feb. 2007. Using the material-point method to model sea ice dynamics. J. Geophys. Res. 112 (C2).

Thorndike, A. S., Rothrock, D. A., Maykut, G. A., Colony, R., 1975. The thickness distribution of sea ice. J. Geophys. Res. 80, 4501–4513.

Tsamados, M., Feltham, D. L., Schroeder, D., Flocco, D., Farrell, S. L., Kurtz, N., Laxon, S. W., Bacon, S., Jan. 2014. Impact of variable atmospheric and oceanic form drag on simulations of arctic sea ice. Journal of Physical Oceanography 44 (5), 1329–1353.

Walters, R. A., Lane, E. M., Hanert, E., 2009. Useful time-stepping methods for the Coriolis term in a shallow water model . Ocean Modelling 28 (1–3), 66–74.

Wang, L. R., Ikeda, M., 2004. A Lagrangian description of sea ice dynamics using the finite element method. Ocean Mod. 7, 21–38.

Weiss, J., 2013. Drift, Deformation, and Fracture of Sea Ice: A Perspective Across Scales. Springer.

Weiss, J., Marsan, D., 2004. Scale properties of sea ice deformation and fracturing. CR Phys. 5 (7), 735–751.

Weiss, J., Schulson, E. M., Oct. 2009. Coulombic faulting from the grain scale to the geophysical scale: Lessons from ice. J. Phys. D: Appl. Phys. 42 (21), 214017.

Weiss, J., Stern, H. L., Schulson, E. M., 2007. Sea ice rheology from in-situ, satellite and laboratory observations: Fracture and friction. Earth Planet. Sci. Lett. 255 (1-2), 1–8.

Symbol	Meaning	units
h	sea ice thickness	m
A	sea ice concentration	-
d	sea ice damage	-
$\boldsymbol{u}$	sea ice velocity	m s^{-1}
$\boldsymbol{\sigma}$	sea ice internal stress	N m^{-2}

Table 1: Variables used in the model

Symbol	Meaning	Values	Units
ρ_a	air density	1.3	kg m^{-3}
c_a	air drag coefficient	0.003	-
θ_a	air turning angle	0	degree
ρ_w	water density	1025	kg m^{-3}
c_w	water drag coefficient	0.004	-
θ_w	water turning angle	25	degrees
ρ_i	ice density	917	kg m^{-3}
ν	Poisson coefficient	0.3	-
μ	internal friction coefficient	0.7	-
Y	elastic modulus	9	GPa
Δx	mean resolution of the mesh	7	km
Δt	time step	800	s
T_d	damage relaxation time	10^{20}	s
c	cohesion parameter	$[8, \underline{4}, 2, 1, 0.5]$	kPa
α	compactness parameter	$-[40, \underline{20}, 10, 0]$	-

Table 2: Parameters used in the model with their values for the simulations presented in this study. Underlined values are for the reference simulation.

c [kPa]	$<\dot{\mathcal{O}}>$ [km^{2}day^{-1}]	$<\dot{\mathcal{C}}>$ [km^{2}day^{-1}]	$<\dot{\mathcal{S}}>$ [km^{2}day^{-1}]	$\delta_{\dot{\mathcal{O}}_{50\%}}$	$\delta_{\dot{\mathcal{C}}_{50\%}}$	$\delta_{\dot{\mathcal{S}}_{50\%}}$
8	15 000	-17 000	86 000	0.06	0.01	0.07
4	15 000	-24 000	106 000	0.06	0.01	0.08
2	15 000	-27 000	117 000	0.09	0.01	0.10
1	17 000	-28 000	129 000	0.10	0.01	0.11
0.5	19 000	-28 000	141 000	0.11	0.01	0.14

Table 3: Values of the total opening, closing and shearing rates computed at the scale of the elements over the last 3 days of simulations using different values of the cohesion parameter c. $\delta_{\dot{\mathcal{O}}_{50\%}}$, $\delta_{\dot{\mathcal{C}}_{50\%}}$ and $\delta_{\dot{\mathcal{S}}_{50\%}}$ are the minimum fractions of the total area needed to accommodate 50% of the total opening, closing and shearing rates, respectively.

c[kPa]	$\beta_{shear}(1)$	a_{shear}	$\beta_{div}(1)$	a_{div}
8	0.04	0.21	0.09	0.22
4	0.04	0.18	0.15	0.23
2	0.05	0.14	0.18	0.18
1	0.07	0.13	0.21	0.11
0.5	0.09	0.11	0.24	0.14

Table 4: Impact of using different values of the cohesion parameter c on the structure function $\beta(q)$, which is well fitted by a quadratic function $\beta(q) = aq^2 + bq$. $\beta(1)$ and a are given for the shear and divergence rates, respectively.

α	$<\dot{\mathcal{O}}>$ [km^{2}day^{-1}]	$<\dot{\mathcal{C}}>$ [km^{2}day^{-1}]	$<\dot{\mathcal{S}}>$ [km^{2}day^{-1}]	$\delta_{\dot{\mathcal{O}}_{50\%}}$	$\delta_{\dot{\mathcal{C}}_{50\%}}$	$\delta_{\dot{\mathcal{S}}_{50\%}}$
-40	22 000	-29 000	109 000	0.05	0.01	0.05
-20	15 000	-24 000	106 000	0.06	0.01	0.08
-10	12 000	-22 000	105 000	0.05	0.01	0.10
0	11 000	-19 000	102 000	0.06	0.02	0.12

Table 5: Values of the total opening, closing and shearing rates computed at the scale of the elements over the last 3 days of simulations using different values of the compactness parameter α. $\delta_{\dot{\mathcal{O}}_{50\%}}$, $\delta_{\dot{\mathcal{C}}_{50\%}}$ and $\delta_{\dot{\mathcal{S}}_{50\%}}$ are the minimum fractions of the total area needed to accommodate 50% of the total opening, closing and shearing rate, respectively.

α	$\beta_{shear}(1)$	a_{shear}	$\beta_{div}(1)$	a_{div}
-40	0.06	0.18	0.18	0.21
-20	0.04	0.18	0.15	0.23
-10	0.04	0.17	0.15	0.21
0	0.04	0.14	0.14	0.20

Table 6: Impact of using different values of the compactness parameter α on the structure function $\beta(q)$, which is well fitted by a quadratic function $\beta(q) = aq^2 + bq$. $\beta(1)$ and a are given for the shear rate and divergence rates, respectively.

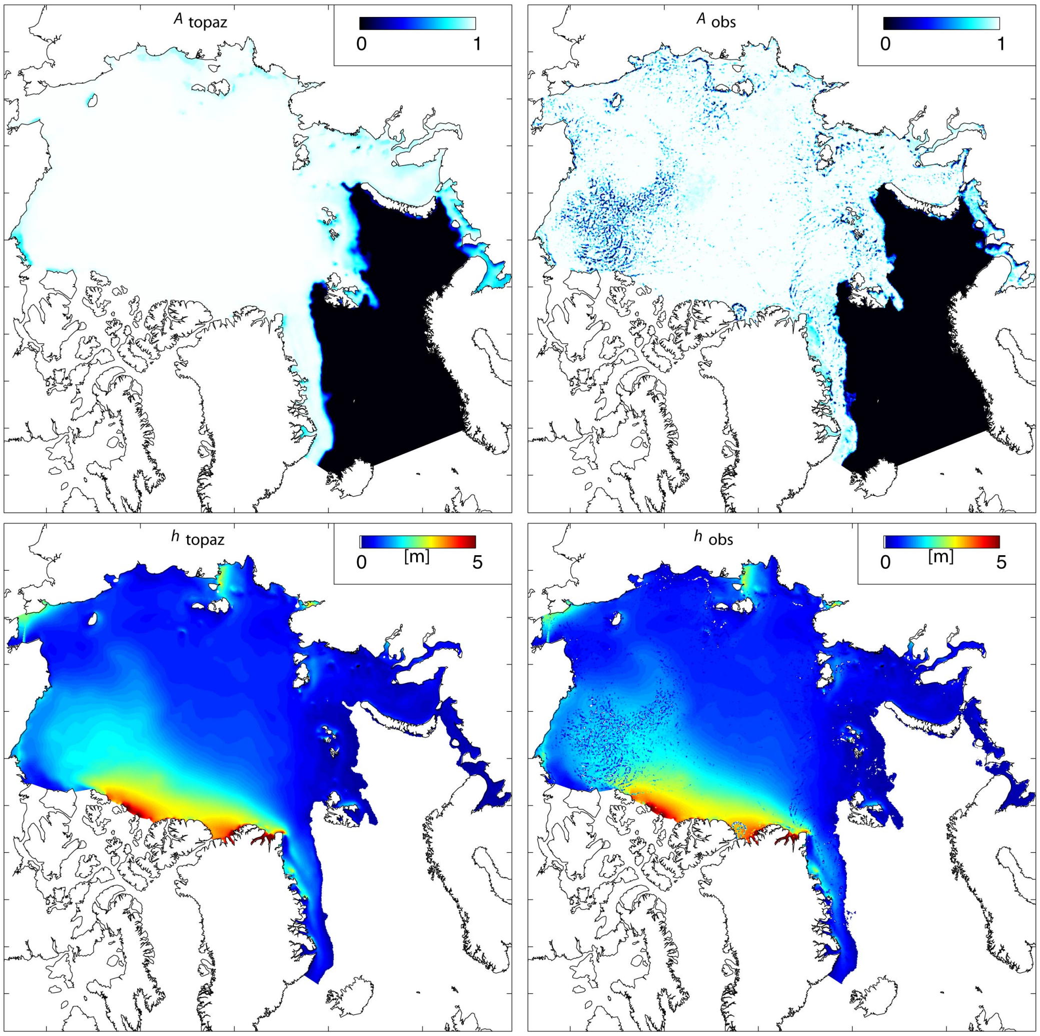

Figure 1: Two sets of sea ice conditions are used to initialize the model (here for the 5th March 2008): either the sea ice concentration (A_{topaz}) and thickness (h_{topaz}) from the TOPAZ reanalysis (left panel), or a combination of the sea ice concentrations A_{tot} and lead area fraction A_{lead} derived from AMSR-E (right panel). The initial sea ice concentration is then defined as $A_{obs} = A_{tot}\,(1 - A_{lead})$ and the initial sea ice thickness is defined as $h_{obs} = h_{topaz}/A_{topaz}A_{obs}$.

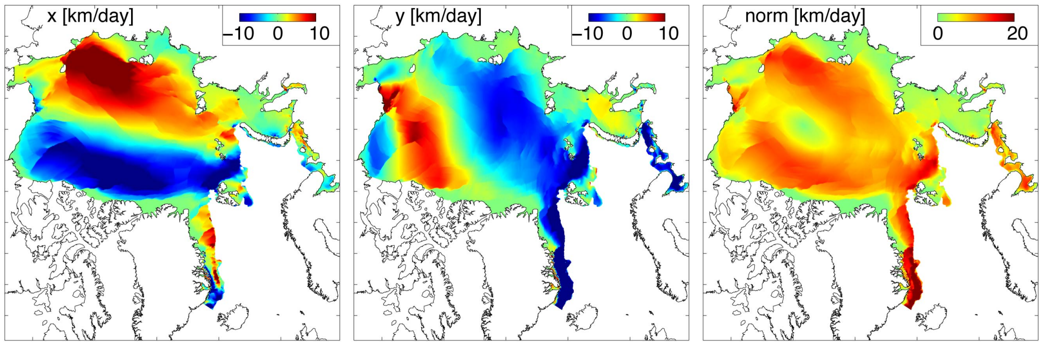

Figure 2: x-component, y-component and norm of the sea ice velocity (in km/day) computed over the last 3 days of the reference simulation (from 12 to 15 March 2008).

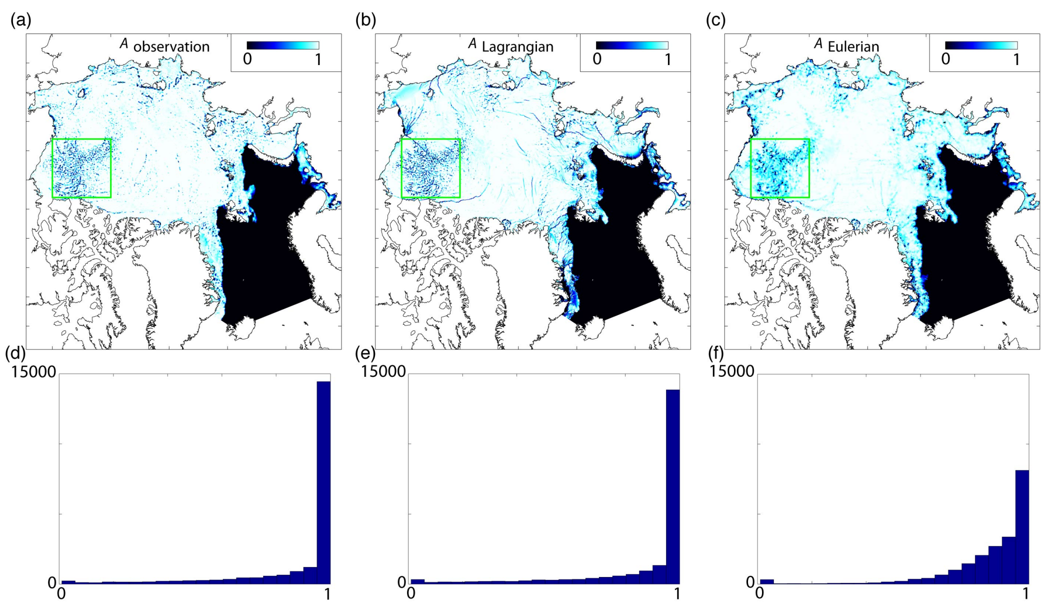

Figure 3: Sea ice concentration fields for the 15th March 2008 from observations (a) and obtained from simulations initialized on the 5th March with A_{obs} and h_{obs} using a Lagrangian advection scheme (b) or an Eulerian upwind advection scheme (c). The corresponding distributions of ice concentration (d, e, f) are computed on an arbitrary region in the Beaufort Sea indicated by a green rectangle. The numerical diffusion produced by the use of the Eulerian upwind scheme significantly impacts the statistics of ice concentration.

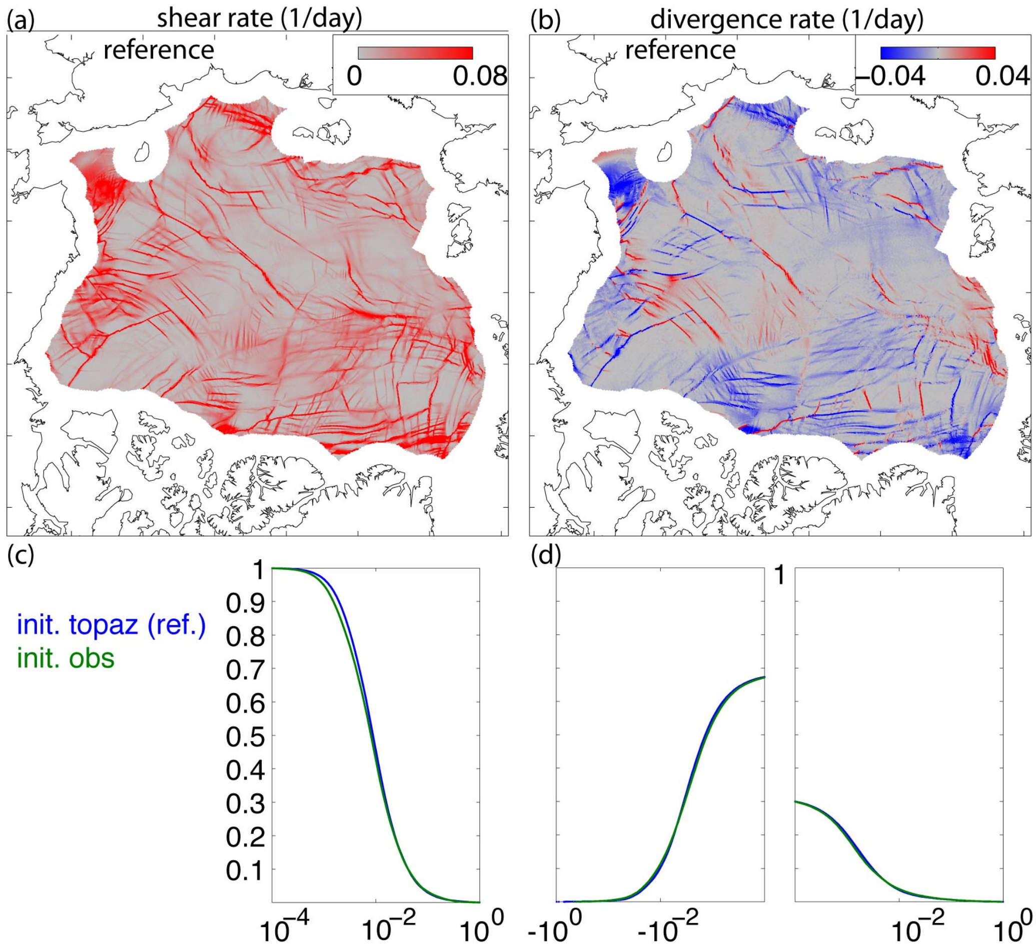

Figure 4: Sea ice (a) shear rate and (b) divergence rate (in 1/day) computed over the last 3 days of the reference simulation (from 12 to 15 March 2008) for all the elements in the Central Arctic that are located at least 150 km from the nearest coasts. The corresponding cumulative distributions (c, d), in other words the probabilities of exceedance, are shown for the reference simulation (i.e., with initial conditions A_{topaz} and h_{topaz}, blue line) and for the simulation with the initial conditions A_{obs} and h_{obs} (green line). In both cases, the cohesion c=4 kPa and the compactness parameter $\alpha = -20$ (see Table 6 for the list of all the parameters).

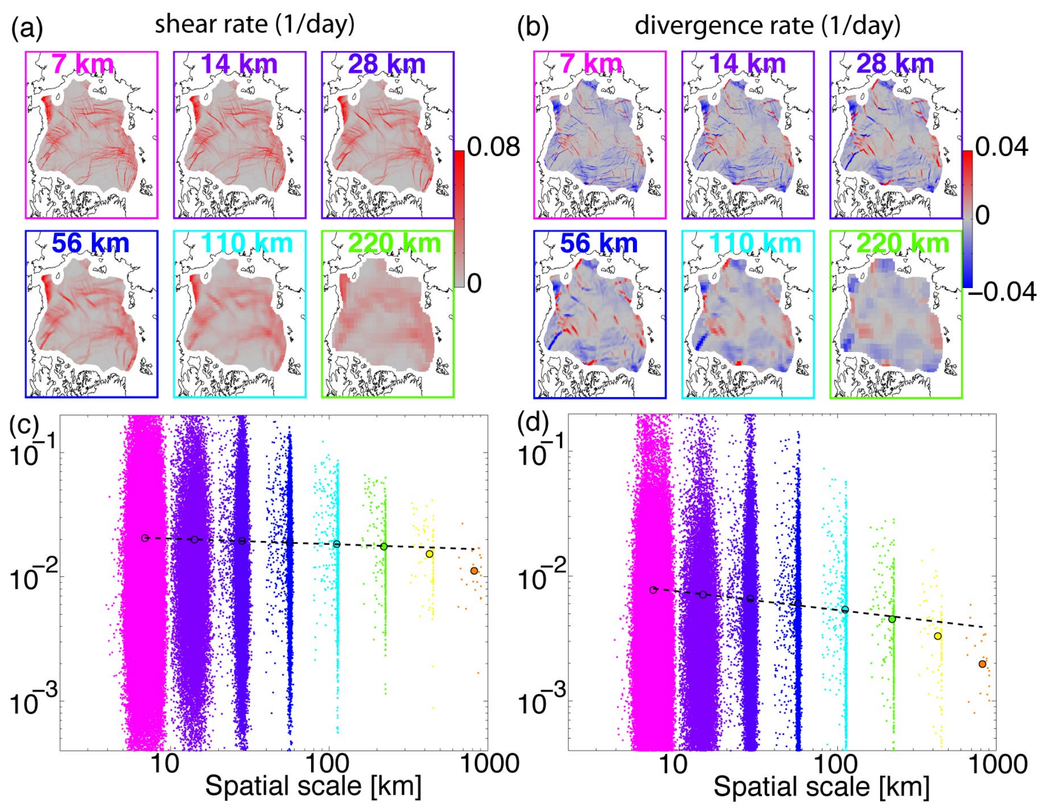

Figure 5: Sea ice (a) shear rate and (b) divergence rate (in 1/day) computed over the last 3 days of the reference simulation (from 12 to 15 March 2008) for spatial scales ranging from 7 to 220 km (each color corresponds to a different scale). The coarse-graining procedure defines boxes of different sizes and compute for each box the mean deformation over all the elements that have their center in the box. The values of the shear rate and divergence rate are then reported as a function of the spatial scale, here defined as the square root of the area covered by the selected elements (c, d, respectively). The mean values are represented by circles and the dashed lines are power law fits of the first six mean values (here, from 7 to 220 km).

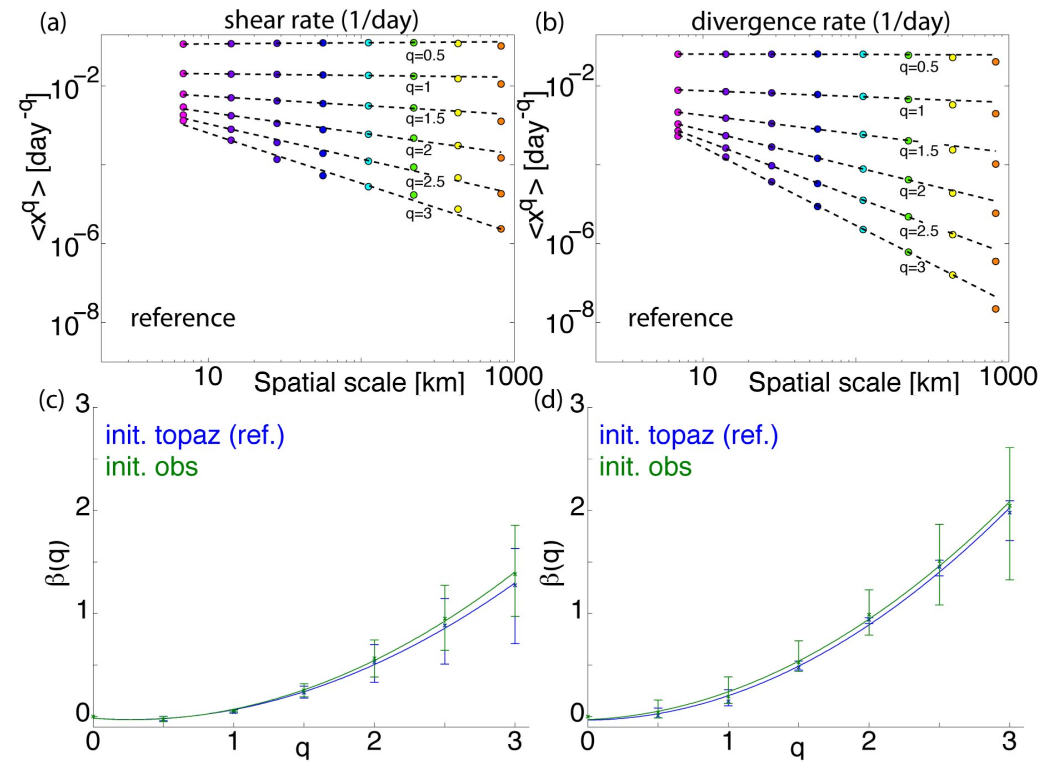

Figure 6: Multifractal analysis: Moments of the deformation rates $< \dot{\epsilon}^q >$ as a function of the scale for $q = 0.5$ to 3, for shear (a) and divergence (b) from the reference simulation. Dashed lines are power law fits of the sixth first values (here, from 7 to 220 km). The slope β of these dashed lines are plotted as a function of the moment order q for the shear (c) and divergence (d) along with the best (in the least-square sense) quadratic fits $\beta(q) = aq^2 + bq$ (solid lines). The curvature a indicates the degree of multifractality. The bars on the graph are not error bars but indicate for each moment order q the minimum and maximum slope β obtained with only two of the six first values.

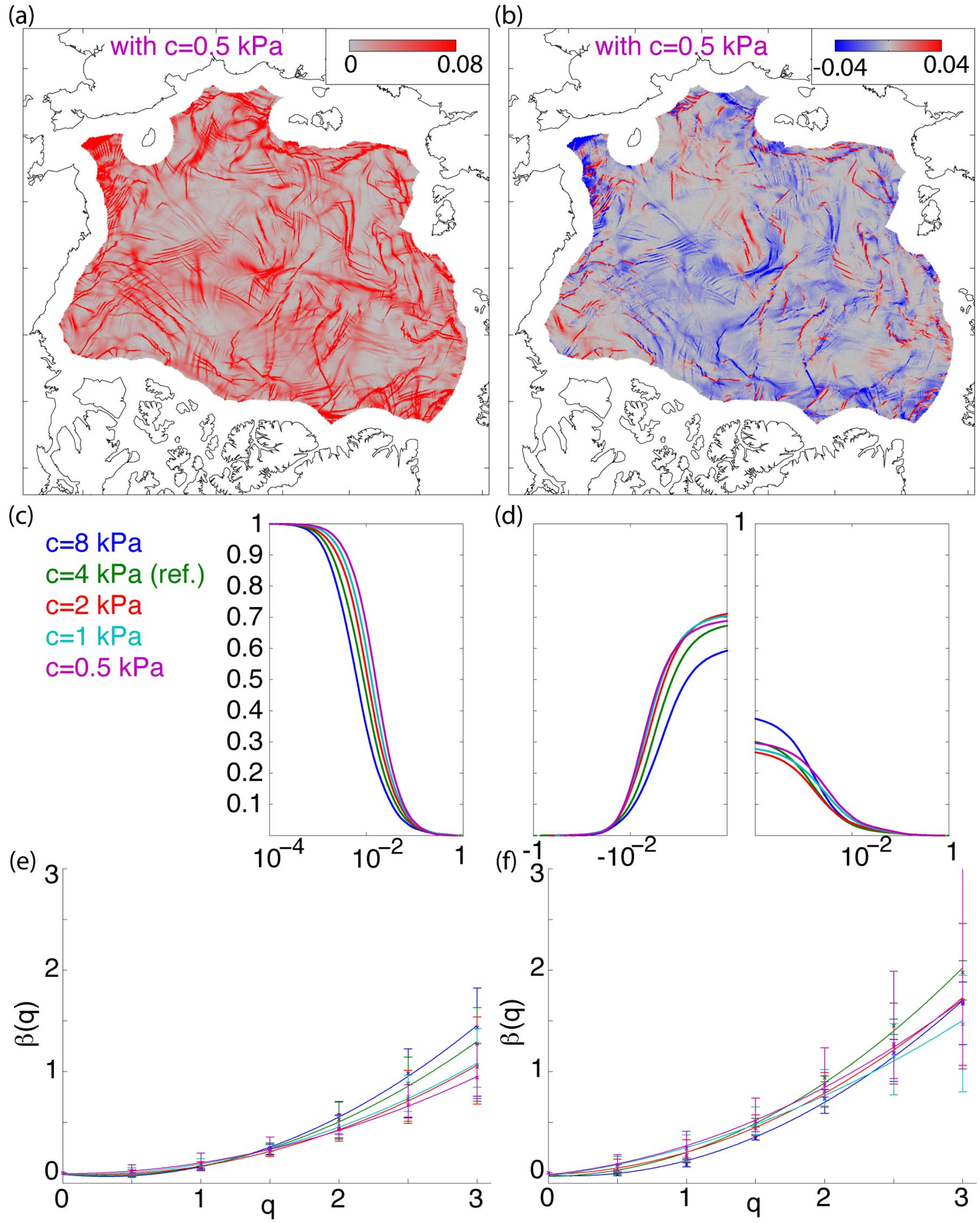

Figure 7: Sea ice (a) shear rate and (b) divergence rate (in 1/day) computed over the last 3 days of the simulation using a cohesion c=0.5 kPa. The corresponding cumulative distributions (c, d) and $\beta(q)$ functions (e, f) are shown for a cohesion parameter equal to 8, 4, 2, 1 and 0.5 kPa.

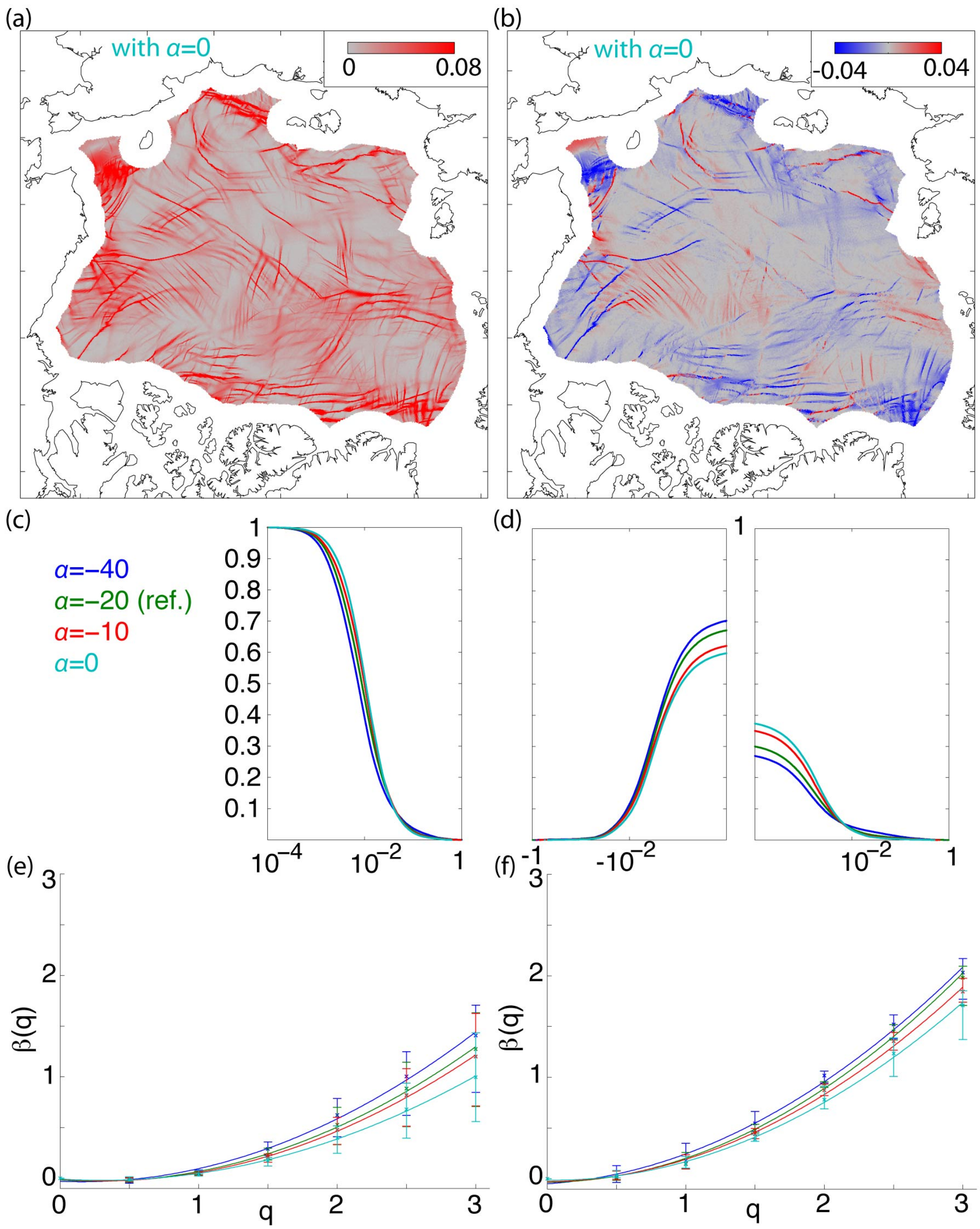

Figure 8: Sea ice (a) shear rate and (b) divergence rate (in 1/day) computed over the last 3 days of the simulation using a compactness parameter $\alpha = 0$. The corresponding cumulative distributions (c, d) and $\beta(q)$ functions (e, f) are shown for a compactness parameter equal to -40, -20, -10 and 0.